PHYSICAL REVIEW D **83,** 084013 (2011)

Characterization of the gravitational wave emission of three black holes

Pablo Galaviz[1,2,*] and Bernd Brügmann[2,†]

[1]*School of Mathematical Science, Monash University, Melbourne, VIC 3800, Australia*
[2]*Theoretical Physics Institute, University of Jena, 07743 Jena, Germany*

(Received 7 January 2011; published 7 April 2011)

We study the gravitational wave emission of three compact objects using post-Newtonian (PN) equations of motion derived from the Arnowitt-Deser-Misner-Hamiltonian formulation, where we include (for the first time in this context) terms up to 2.5 PN order. We perform numerical simulations of a hierarchical configuration of three compact bodies in which a binary system is perturbed by a third, lighter body initially far away from the binary. The relative importance of the different PN orders is examined. We compute the waveform in the linear regime considering mass quadrupole, current quadrupole and mass octupole contributions. Performing a spherical harmonic decomposition of the waveforms we find that from the $l = 3$ modes it is possible to extract information about the third body, in particular, the period, eccentricity of its orbit, and the inclination angle between the inner and outer binary orbits.

DOI: 10.1103/PhysRevD.83.084013 PACS numbers: 04.25.Nx, 04.30.Db, 04.70.Bw

I. INTRODUCTION

In the near future gravitational wave detectors will open a new branch on astronomy beyond electromagnetism and particles. In order to extract astrophysical information from the waves it is crucial to model the source in an accurate way. One of the parameters to determine is the number of bodies which generate the waves. Some configurations of three bodies can produce particular periodic waveforms with distinctive features, e.g. [1]. On the other hand, Lagrange's triangle solution produces a quadrupole waveform which is identical to the one produced by a binary system [2]. However, it is possible to distinguish between a binary system and a triple one by considering the octupole part of the waveform [3]. Lagrange's solution is stable only if one of the bodies holds more than 95% of the total mass [4]. For three-body systems of comparable masses there are stable configuration in which it is possible to characterize the system by looking at the waveform. In this work we consider *Jacobian systems*, in which the three-body configuration is composed of two parts, a clearly defined binary and a third body orbiting far away. We will refer to this kind of system also as a hierarchical system.

Several models of three or more black holes were recently studied from the astrophysical point of view. Hierarchical three black hole configurations interacting in a galactic core were studied by several authors. For example in [5–7] some configurations of intermediate-mass black holes with different mass ratios were considered. The inclusion of gravitational radiation was done via an effective force which includes 1 PN (post-Newtonian) and 2.5 PN corrections to the binary dynamics. The configurations consist of a binary system in a quasicircular orbit and a third black hole approaching from a distance around 200 times the binary separation. The initial eccentricity was specified in a random way. N-body simulations of dynamical evolution of triple equal-mass supermassive black holes in a galactic nuclei were performed in [8]. The method includes an effective force with gravitational radiation terms and galaxy halo interactions. In [9] the dynamics of repeated triple supermassive black hole interactions in galactic nuclei with several mass ratios and eccentricities were considered. The simulations were performed using Newtonian dynamics with corrections through an additional force which includes 2.5 PN corrections to the binary dynamics and stellar dynamical friction. Other astrophysical applications of multiple black hole simulations include, for example, three-body kicks [10,11] and binary-binary encounters (see e.g. [12–16]).

The first complete simulations using general-relativistic numerical evolutions of three black holes were presented in [17,18]. These recent simulations show that the dynamics of three compact objects display a qualitatively different behavior than the Newtonian dynamics. In [19] the sensitivity of fully relativistic evolutions of three and four black holes to changes in the initial data was examined, where the examples for three black holes are some of the simpler cases already discussed in [17,18]. The apparent horizon and the event horizon of multiple black holes have been studied in [20–22]. Although fully general-relativistic simulations are available, they are limited to only a small number of orbits for small separations of the black holes.

In the present work we study three-body systems with PN methods, where the main technical novelty is the inclusion of the 2.5 PN terms in the orbital dynamics. We do not consider compact objects with spin, although recently the knowledge of Hamiltonian up to 2.5 PN was completed with the computation of a next-to-leading order spin-orbit and spin-spin Hamiltonian [23–25]

*Pablo.Galaviz@monash.edu
†Bernd.Bruegmann@uni-jena.de

Using post-Newtonian techniques, it is currently possible to describe the dynamics of n compact objects without spin up to 3.5 PN order (see e.g. [26–32]), although explicit and closed expressions for the terms required for our purpose are not available for arbitrary n. For binary systems the Arnowitt-Deser-Misner (ADM) Hamiltonian has been specialized up to 3.5 PN order [33]. For three bodies there are explicit formulas up to 2.5 PN order, with the final key integral performed in [34] (see also Appendix A and [35]; see [36] for an alternative discussion where the final result is not as yet explicit). For four compact objects, the same degree of explicitness has not been obtained, see e.g. [37] on which [34] is based where the integral (C.2) must be computed for four bodies, and also Appendix D of [38]. In the ADM-Hamiltonian formalism the resulting equations of motion exactly conserve the constants of motion. For numerical simulations this represents an advantage with respect to other post-Newtonian approaches, since the constants of motion can be tracked and their constancy continually checked.

Periodic solutions were studied using the 1 PN and 2 PN approximation in [35,39,40]. Examples of three compact bodies in a collinear configuration were considered in [41,42], and Lagrange's equilateral triangular solution was studied including 1 PN effects in [43]. In [44], the stability of the Lagrangian points in a black hole binary system was studied in the test particle limit, for which radiation effects were modeled by a drag force.

The most likely source of gravitational waves are binary compact objects. Recently it was shown that the probability that more than two black holes interact in the strongly relativistic regime is, not surprisingly, very small [45]. For practical purposes the creation of gravitational waveform templates for gravitational wave detectors is naturally focused on binary systems, and even binary systems can produce complicated waveforms when taking into account spinning black holes and eccentric orbits, e.g. [46].

Nevertheless, it remains an interesting question of principle what additional wave phenomena are possible for more than two compact objects. The waveform characterization of three or more compact objects is complementary to the study of binary systems. For a three-body system the complexity of the orbits can reveal properties of the waves which for a binary system are hidden. As we will demonstrate for a hierarchical system, from the $l = 3$ modes of the gravitational wave it is possible to extract information about the third body, particularly the period, eccentricity of its orbit and the inclination angle between the inner and outer binary orbits.

The paper is organized as follows. In Sec. II, we summarize the equation of motion up to 2.5 post-Newtonian approximation for three bodies. This is followed by a discussion of gravitational radiation in the linear regime and the multipole expansion of the gravitational waves. In Sec. III A, we describe the numerical techniques used to solve the equation of motion and we present some results for test cases. The perturbation of a binary system by a third object is presented in Sec. III B, where we perform numerical experiments in order to characterize the waveform. We conclude in Sec. IV.

Notation and units

We employ the following notation: $\vec{x} = (x_i)$ denotes a point in the three-dimensional Euclidean space $\mathbb{R}^3$, letters $a, b, \ldots$ are particle labels. We define $\vec{r}_a := \vec{x} - \vec{x}_a$, $r_a := |\vec{r}_a|$, $\hat{n}_a := \vec{r}_a/r_a$; for $a \neq b$, $\vec{r}_{ab} := \vec{x}_a - \vec{x}_b$, $r_{ab} := |\vec{r}_{ab}|$, $\hat{n}_{ab} := \vec{r}_{ab}/r_{ab}$; here $|\cdot|$ denotes the length of a vector. The mass parameter of the a-th particle is denoted by m_a, with $M = \sum_a m_a$. Summation runs from 1 to 3. The linear momentum vector is denoted by $\vec{p}_a$. A dot over a symbol, as in $\dot{\vec{x}}$, means the total time derivative, and partial differentiation with respect to x^i is denoted by ∂_i.

In order to simplify the calculations it is useful to define dimensionless variables (see e.g. [47]). We use as basis quantities for the Newtonian and post-Newtonian calculation the gravitational constant G, the speed of light c and the total mass of the system M. Using derived constants for time $\tau = MG/c^3$, length $l = MG/c^2$, linear momentum $\mathcal{P} = Mc$ and energy $\mathcal{E} = Mc^2$ we construct dimensionless variables. The physical variables are related with the dimensionless variables by means of a scaling, for example, denoting with capital letters the physical variables with the usual dimensions and with lowercase the dimensionless variable we define for a particle a its position $\vec{x}_a := \vec{X}_a/l$, linear momentum $\vec{p}_a := \vec{P}_a/\mathcal{P}$ and mass $m_a = M_a/M$ (notice that $m_a < 1$, $\forall a$).

II. EQUATIONS OF MOTION

In the ADM post-Newtonian approach it is possible to split the Hamiltonian in a series with coefficients which are inverse powers of the speed of light (see e.g. [27,48])

$$\mathcal{H}_{\leq 2.5} = \mathcal{H}_0 + c^{-2}\mathcal{H}_1 + c^{-4}\mathcal{H}_2 + c^{-5}\mathcal{H}_{2.5}. \quad (1)$$

Here each term of the Hamiltonian $c^n \mathcal{H}_{n/2}$ is a quantity with a dimension of energy, and we write it explicitly with factors of c. The dimensionless Hamiltonian is given by $H_{n/2} = c^n \mathcal{H}_{n/2}/\mathcal{E}$. For each term we calculate the equations of motion

$$(\dot{x}^i_a)_n = \frac{\partial H_n}{\partial p^i_a}, \quad (2)$$

$$-(\dot{p}^i_a)_n = \frac{\partial H_n}{\partial x^i_a}, \quad (3)$$

where the equations of motion up to 2.5 PN approximation are

$$\dot{\vec{x}}_a = (\dot{\vec{x}}_a)_0 + (\dot{\vec{x}}_a)_1 + (\dot{\vec{x}}_a)_2 + (\dot{\vec{x}}_a)_{2.5}, \quad (4)$$

$$\dot{\vec{p}}_a = (\dot{\vec{p}}_a)_0 + (\dot{\vec{p}}_a)_1 + (\dot{\vec{p}}_a)_2 + (\dot{\vec{p}}_a)_{2.5}. \quad (5)$$

The first term in (1) is the Hamiltonian for n particles interacting under Newtonian gravity,

$$H_0 = \frac{1}{2}\sum_a^n \frac{\vec{p}_a^2}{m_a} - \frac{1}{2}\sum_{a,b\neq a}^n \frac{m_a m_b}{r_{ab}}, \tag{6}$$

with $\vec{p}_a = m_a \dot{\vec{x}}_a^2$. The inclusion of post-Newtonian corrections enriches the phenomenology of the system.

A. Post-Newtonian equations of motion up to 2.5 order

The first post-Newtonian correction to the equations of motion is discussed extensively in the literature (see e.g. [27,49]). The three-body Hamiltonian at first and second post-Newtonian order is given in Appendix A. The equations of motion for the first post-Newtonian order are given by (2), (3), and (A1). For particle a we obtain

$$(\dot{\vec{x}}_a)_1 = -\frac{\vec{p}_a^2}{2m_a^3}\vec{p}_a - \frac{1}{2}\sum_{b\neq a}\frac{1}{r_{ab}}\left(6\frac{m_b}{m_a}\vec{p}_a - 7\vec{p}_b - (\hat{n}_{ab}\cdot\vec{p}_b)\hat{n}_{ab}\right), \tag{7}$$

$$\begin{aligned}(\dot{\vec{p}}_a)_1 = &-\frac{1}{2}\sum_{b\neq a}\Bigg[3\frac{m_b}{m_a}\vec{p}_a^2 + 3\frac{m_a}{m_b}\vec{p}_b^2 - 7(\vec{p}_a\cdot\vec{p}_b) \\ &- 3(\hat{n}_{ab}\cdot\vec{p}_a)(\hat{n}_{ab}\cdot\vec{p}_a)\Bigg]\frac{\hat{n}_{ab}}{r_{ab}^2} \\ &+ \sum_{b\neq a}\sum_{c\neq a}\frac{m_a m_b m_c}{r_{ab}^2 r_{ac}}\hat{n}_{ab} + \sum_{b\neq a}\sum_{c\neq b}\frac{m_a m_b m_c}{r_{ab}^2 r_{bc}}\hat{n}_{ab} \\ &- \frac{1}{2}\sum_{a\neq b}\Bigg[\frac{(\hat{n}_{ab}\cdot\vec{p}_b)\vec{p}_a + (\hat{n}_{ab}\cdot\vec{p}_a)\vec{p}_b}{r_{ab}^2}\Bigg].\end{aligned} \tag{8}$$

For the second post-Newtonian approximation the equations of motion are calculated using (2), (3), and (A2). For brevity we do not display the explicit equations.

Following [26,33] we obtain equations of motion from the 2.5 PN Hamiltonian in the ADM gauge. The general 2.5 PN Hamiltonian is

$$H_{2.5} = \frac{1}{45}\dot{\chi}_{(4)ij}(\vec{x}_{a'}, \vec{p}_{a'}; t)\chi_{(4)ij}(\vec{x}_a, \vec{p}_a), \tag{9}$$

where the auxiliary function $\chi_{(4)ij}$ is defined by

$$\begin{aligned}\chi_{(4)ij}(\vec{x}_a, \vec{p}_a) := &\sum_a \frac{2}{m_a}(\vec{p}_a^2\delta_{ij} - 3p_{ai}p_{aj}) \\ &+ \sum_a\sum_{b\neq a}\frac{m_a m_b}{r_{ab}}(3n_{abi}n_{abj} - \delta_{ij}).\end{aligned} \tag{10}$$

Our expressions differ from [26,33] due to a different choice of units. The explicit form of the derivative in (9) is

$$\begin{aligned}\dot{\chi}_{(4)ij}(\vec{x}_{a'}, \vec{p}_{a'}) = &\sum_{a'}\frac{2}{m_{a'}}[2(\dot{\vec{p}}_{a'}\cdot\vec{p}_{a'})\delta_{ij} - 3(\dot{p}_{a'i}p_{a'j} + p_{a'i}\dot{p}_{a'j})] \\ &+ \sum_{a'}\sum_{b'\neq a'}\frac{m_{a'}m_{b'}}{r_{a'b'}^2}[3(\dot{r}_{a'b'i}n_{a'b'j} + n_{a'b'i}\dot{r}_{a'b'j}) \\ &+ (\hat{n}_{a'b'}\cdot\dot{\vec{r}}_{a'b'})(\delta_{ij} - 9n_{a'b'i}n_{a'b'j})].\end{aligned} \tag{11}$$

We denote the retarded variables by primed quantities. The position and momentum appearing in Eq. (11) are not affected by the derivative operators given by (2) and (3), and only after calculating those derivatives we identify positions and momenta inside and outside the transverse-traceless variables (i.e. the primed and unprimed quantities). We replace the time derivatives of the primed coordinates and positions given in Eq. (11) by the 1 PN equations of motion Eqs. (7) and (8).

The equations of motion for 2.5 PN are given in short hand by

$$(\dot{\vec{x}}_a)_{2.5} = \frac{1}{45}\dot{\chi}_{(4)ij}(\vec{x}_a, \vec{p}_a; (\dot{\vec{x}}_a)_1, (\dot{\vec{p}}_a)_1, t)\frac{\partial}{\partial\vec{p}_a}\chi_{(4)ij}(\vec{x}_a, \vec{p}_a), \tag{12}$$

$$\begin{aligned}(\dot{\vec{p}}_a)_{2.5} = &-\frac{1}{45}\dot{\chi}_{(4)ij}(\vec{x}_a, \vec{p}_a; (\dot{\vec{x}}_a)_1, (\dot{\vec{p}}_a)_1, t) \\ &\times\frac{\partial}{\partial\vec{x}_a}\chi_{(4)ij}(\vec{x}_a, \vec{p}_a).\end{aligned} \tag{13}$$

Given initial values for $\vec{x}_a$ and $\vec{p}_a$ of each particle it is possible to integrate the resulting equations of motion numerically.

B. Gravitational radiation in the linear regime

We consider leading order and next-to-leading order gravitational waves calculated using trajectories which contain post-Newtonian corrections. We compute the gravitational waveforms for a given observational direction, and alternatively we calculate the multipole decomposition which allows us to reconstruct the waves for an arbitrary direction. The inclusion of post-Newtonian corrections to the gravitational waveforms is a topic for future research in the three-compact-body problem.

1. Quadrupole and octupole formulas

Here we summarize the formulas for quadrupole and octupole mass radiation and for current quadrupole radiation (for a review see e.g. [48,50]). The second and third mass moments are defined by

$$M^{ij}(t) = \int T^{00}(\vec{x}, t)x^i x^j d^3x, \tag{14}$$

$$M^{ijk}(t) = \int T^{00}(\vec{x}, t)x^i x^j x^k d^3x. \tag{15}$$

The second moment of the momentum density is

$$P^{i,jk}(t) = \int T^{0i}(\vec{x}, t)x^j x^k d^3x. \quad (16)$$

For n point particles

$$T^{\mu\nu}(\vec{x}, t) = \sum_a \frac{p_a^\mu p_a^\nu}{\gamma_a m_a}\delta^3(\vec{x} - \vec{x}_a(t)), \quad (17)$$

where $\gamma_a := (1 - \vec{p}_a^2)^{-1/2}$ is the Lorentz factor, and $p_a^\mu := \gamma_a(m_a, \vec{p}_a)$ is the four-momentum. In this case Eqs. (14)–(16) reduce to

$$M^{ij}(t) = \sum_a \gamma_a m_a x_a^i(t)x_a^j(t), \quad (18)$$

$$M^{ijk}(t) = \sum_a \gamma_a m_a x_a^i(t)x_a^j(t)x_a^k(t), \quad (19)$$

$$P^{i,jk}(t) = \sum_a p_a^i(t)x_a^j(t)x_a^k(t). \quad (20)$$

In the following we consider the case where $|\vec{p}_a| \ll 1$, $\gamma_a \simeq 1$.

The mass quadrupole and octupole moment are given by

$$\mathcal{Q}^{ij}(t) = M^{ij} - \frac{1}{3}\delta^{ij}M^{kk},$$

$$\mathcal{O}^{ijk}(t) = M^{ijk} - \frac{1}{5}(\delta^{ij}M^{llk} + \delta^{ik}M^{ljl} + \delta^{jk}M^{ill}),$$

where repeated indices mean summation from 1 to 3. The current quadrupole is given by

$$\mathcal{C}^{k,lm}(t) = P^{k,lm} + P^{l,km} - 2P^{m,kl}. \quad (21)$$

A projection tensor into the plane normal to the direction of wave propagation, $\hat{n} = (\sin\theta\sin\phi, \sin\theta\cos\phi, \cos\theta)$, is defined by

$$\mathcal{P}_{ij} := \delta_{ij} - n_i n_j, \quad (22)$$

$$\Lambda_{ijkl}(\hat{n}) := \mathcal{P}_{ik}\mathcal{P}_{jl} - \frac{1}{2}\mathcal{P}_{ij}\mathcal{P}_{kl}. \quad (23)$$

The mass quadrupole and octupole waveforms are given by

$$h_{ij}^{TT}(\vec{x}, t)_{\mathrm{MQ}} = \frac{2}{r}\Lambda_{ijkl}(\hat{n})\ddot{\mathcal{Q}}^{kl}(t - r), \quad (24)$$

$$h_{ij}^{TT}(\vec{x}, t)_{\mathrm{MO}} = \frac{2}{3r}\Lambda_{ijkl}(\hat{n})n_m\dddot{\mathcal{O}}^{klm}(t - r), \quad (25)$$

and the current quadrupole contribution to the waveform is

$$h_{ij}^{TT}(\vec{x}, t)_{\mathrm{CQ}} = \frac{4}{3r}\Lambda_{ijkl}(\hat{n})n_m\ddot{\mathcal{C}}^{k,lm}. \quad (26)$$

The total contribution on the waveform is given by

$$h_{ij}^{TT}(\vec{x}, t) = h_{ij}^{TT}(\vec{x}, t)_{\mathrm{MQ}} + h_{ij}^{TT}(\vec{x}, t)_{\mathrm{CQ}} + h_{ij}^{TT}(\vec{x}, t)_{\mathrm{MO}} + \ldots. \quad (27)$$

where … means additional multipoles. Assuming that the wave propagates in the $\hat{z}$-direction, then $h_+ = h_{11}^{TT}$ and $h_\times = h_{12}^{TT}$. For an arbitrary direction $\hat{n}(\theta, \phi)$ we have to perform a rotation of the axes in order to identify the polarization with the h_{11}^{TT} and h_{12}^{TT} components.

We decompose h_+ and $h_\times$ into modes using spherical harmonics with spin-weight minus two,

$$h_+ - ih_\times = \sum_l \sum_{m=-l}^{l} {}_{-2}Y_m^l(\Theta, \Phi)\mathrm{h}_l^m, \quad (28)$$

where

$${}_sY_m^l(\Theta, \Phi) := (-1)^s\sqrt{\frac{2l+1}{4\pi}}d_{m(-s)}^l(\Theta)\mathrm{e}^{im\Phi}, \quad (29)$$

$$d_{ms}^l(\Theta) := \sum_{t=C_1}^{C_2}\frac{(-1)^t[(l+m)!(l-m)!(l+s)!(l-s)!]^{1/2}}{(l+m-t)!(l-s-t)!t!(t+s-m)!} \times (\cos\Theta/2)^{2l+m-s-2t}(\sin\Theta/2)^{2t+s-m}, \quad (30)$$

with $C_1 = \max(0, m - s)$ and $C_2 = \min(l + m, l - s)$. Using the orthonormality of the spherical harmonics it is possible to compute h_m^l by

$$\mathrm{h}_m^l = \int_0^{2\pi}\int_0^{\pi} {}_{-2}\bar{Y}_m^l(\theta, \pi/2 - \phi)(h_+ - ih_\times)d\Omega, \quad (31)$$

where $d\Omega = \sin\theta d\theta d\phi$.

III. SIMULATIONS AND RESULTS

A. Numerical integration

We solved the equations of motion numerically using MATHEMATICA 7.0 [51]. We used the built-in low-level functions of the *NDSolve* routine with a "double-step" method using as subalgorithm the "explicit midpoint" method. We divided long simulations into substeps in order to store the result from time to time and to avoid saturating the random-access memory. With this approach we can produce accurate numerical solutions of the equations of motion. For our purpose the performance of MATHEMATICA solving the ordinary differential equation system is not an issue (see the performance and accuracy tests at the end of this section).

An important issue in the numerical integration of a three-body system arises when two of the bodies come very close to each other. Adaptive step size methods can automatically maintain the necessary accuracy to properly resolve the orbits in the close interaction, but issues of efficiency arise. For the Newtonian system a number of techniques have been developed that address problems with accuracy and efficiency, see e.g. [52–56] and references therein. For our PN evolutions, efficiency was not an issue, and furthermore the equations of motion are not valid for arbitrarily small separation anyway. What is of relevance here is a convenient criterion of when to stop the evolution. We monitor the absolute value of each conservative part of the Hamiltonian (1) relative to the sum of the absolute values,

$$H_i^{\%} := 100\left(\frac{|H_i|}{|H_0| + |H_1| + |H_2|}\right). \tag{32}$$

We stop the simulation when the contribution of the first post-Newtonian correction is larger than 10%.

In the remainder of this section we report on several tests that allow us to estimate the numerical errors. We use the Lagrangian equilateral triangle solution to compare the numerical with an analytical solution. In Lagrange's solution each body is sitting in one corner of an equilateral triangle (see e.g. [57]). We set the side of such triangle to $L = 1000$, the mass ratio to 1:2:3, and the eccentricity to zero. Then each body follows a circular orbit (with different radii) around the center of mass. The solution in this case is not stable [4], however for circular orbits we can compute the waveforms and compare with the analytical expressions [3].

In Fig. 1, we show the relative variation of the Hamiltonian

$$\Delta H := \frac{H(0) - H(t)}{H(0)}, \tag{33}$$

and for each body the relative variation of the position with respect to the center of mass. The variation of the Hamiltonian is small (close to machine accuracy), however the error in the orbits grows fast, breaking the regular trajectory. In this case, after seven orbits the numerical solution fails. The waves exhibit a similar behavior. In Fig. 2, we show the error for each polarization of the waveforms (24)–(26). The error is defined as the absolute value of the difference between the numerical calculation and the analytical expression. The mass octupole exhibits a noisy error due to the complicated nature of the analytical expression. On the other hand, it seems that the error in the mass quadrupole starts growing before the errors in the mass octupole and current quadrupole. By looking at the

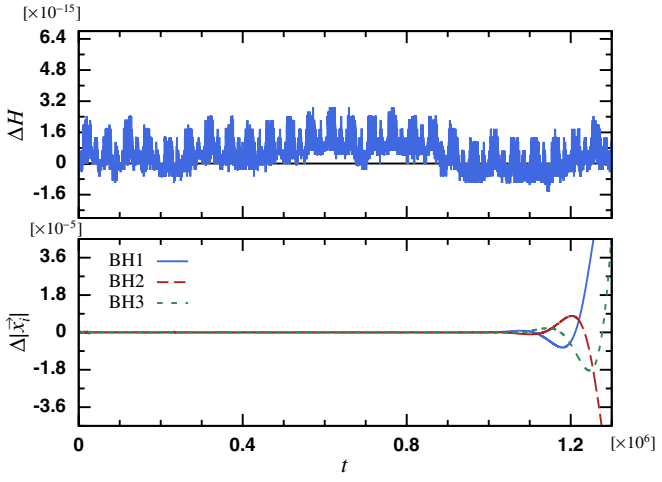

FIG. 1 (color online). Test using Lagrange's equilateral solution of the Newtonian three-body problem. Shown is the relative variation of the Hamiltonian (top) and the relative change in the orbits (bottom).

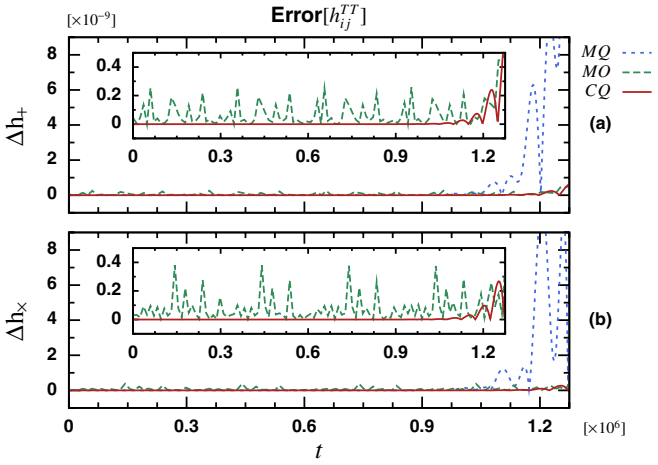

FIG. 2 (color online). Test using Lagrange's equilateral solution of the Newtonian three-body problem. Shown is the absolute value of the difference between the analytical expression and the numerical calculation for the mass quadrupole, mass octupole and the current quadrupole for each polarization of the waveform. The insets show the mass octupole and the current quadrupole.

analytical expressions this fact can be explained as follows (see Eqns. (B5)–(B10)). The mass quadrupole part contains a factor $a^2\omega^2$ (where a is the separation of the bodies and ω the orbital frequency). The mass octupole and current quadrupole have a factor $a^3\omega^3$. In terms of a the factors reduce to a^{-1} and $a^{-3/2}$ respectively. A small change in the orbit is visible at a smaller length scale, and then the growth in the waveforms seems to be delayed.

We reproduce a few of the results from [35], specifically the simulation of the equal-mass Moore's figure eight [39], which includes first and second post-Newtonian corrections. Our choice of method was guided by numerical experiments to minimize the numerical error in this example. With the double-step, midpoint method we obtain fluctuations of the Hamiltonian of 10^{-14} (see Fig. 3), while other methods and parameter settings can show a significantly larger error.

We tested our n-body 2.5 PN equations of motion for the case $n = 2$, i.e. for binary systems. The variation of the semimajor axis and of the eccentricity of a binary system due to the gravitational radiation is given by [58]

$$\frac{da}{dt} = -\frac{64}{5}\frac{m_1 m_2}{a^3(1-e^2)^{7/2}}\left(1 + \frac{73}{24}e^2 + \frac{37}{96}e^4\right), \tag{34}$$

$$\frac{de}{dt} = -\frac{304}{15}\frac{m_1 m_2}{a^4(1-e^2)^{5/2}}\left(e + \frac{121}{304}e^3\right). \tag{35}$$

We tested the 2.5 PN equations of motion (12) and (13) by comparison with direct numerical integration of the Eqs. (34) and (35). The test was performed with two different binaries, one with initial eccentricity $e_0 = 0.1$ and one with $e_0 = 0.5$. In both cases we set $m_1 = 2m_2$, $a_0 = 160$.

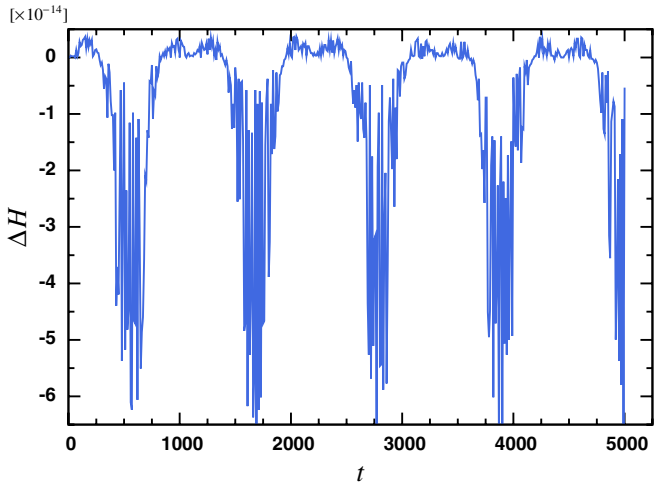

FIG. 3 (color online). Moore's figure eight solution. Relative variation of the Hamiltonian for a solution which includes 2 PN corrections.

The numerical integration of the 2.5 PN equations agree very well with the result provided by the numerical integration of (34) and (35). We calculate the eccentricity of our orbits with the Newtonian formula

$$e = \sqrt{1 + \frac{2l^2 H_c}{(m_1 m_2)^3}}, \tag{36}$$

where l is the magnitude of the total angular momentum and H_c is the value of the conservative part of the Hamiltonian. The apoapsis (the maximum separation of the two bodies) is related to the semimajor axis by $r_{\rm ap} = a(1 + e)$. For simplicity we compare in the upper panel of Fig. 4 the relative variation of $r_{\rm ap}$ to its initial value and in the lower panel we show the variation of the eccentricity.

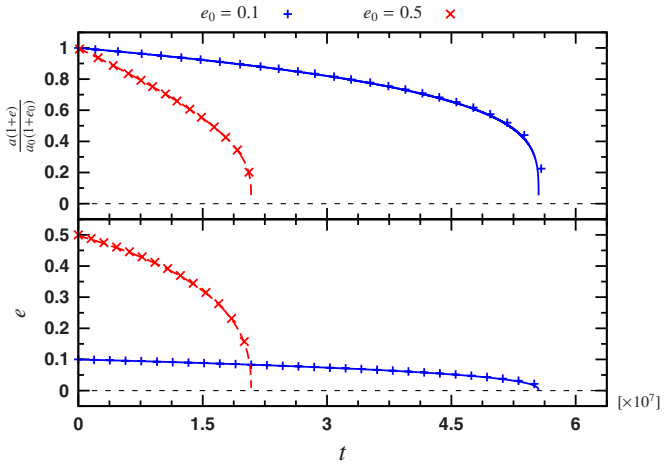

FIG. 4 (color online). Binary system with 2.5 PN radiation. Top: Relative variation of the apoapsis of the two bodies. Bottom: eccentricity variation; comparison of our numerical result (solid and dashed lines) with the numerical integration of (34) and (35) (marks + and ×) for two initial eccentricities.

In order to test the code for long evolutions of three bodies we use Hénon's criss-cross solution [35,59,60]. This solution is stable with respect to a wide range of perturbations [61]. We evolve the equal-mass criss-cross solution for around 10^3 orbits for ad-hoc initial parameters. In our system of units,

$$\vec{x}_1(0) = 1.07590\lambda^2\hat{x}, \quad \vec{p}_1(0) = 3^{-3/2}\cdot 0.19509\lambda^{-1}\hat{y},$$
$$\vec{x}_2(0) = -0.07095\lambda^2\hat{x}, \quad \vec{p}_2(0) = -3^{-3/2}\cdot 1.23187\lambda^{-1}\hat{y},$$
$$\vec{x}_3(0) = -1.00496\lambda^2\hat{x}, \quad \vec{p}_3(0) = 3^{-3/2}\cdot 1.03678\lambda^{-1}\hat{y},$$

where $\hat{x}$, $\hat{y}$ and $\hat{z}$ are the unitary basis vectors in Cartesian coordinates, and λ is a scaling factor (for our simulation $\lambda = 10$). Notice that for this test we use the parameters given in [61] with the scaling factor λ, and doing a change of variables from initial velocity to initial momentum. Therefore, we are not including post-Newtonian corrections to the initial parameters. In Fig. 5 we plot the relative variation of the Hamiltonian for the evolution using a Newtonian potential and the corresponding Hamiltonian variation for evolutions which include 2 and 2.5 PN corrections. As is expected the variation of the Hamiltonian in the 2.5 PN case is huge compared to the conservative case, and the bodies separate after around $t = 7.825 \times 10^6$. The inner panel in Fig. 5 shows a detail of the conservative part. In this case the 2.5 PN dynamics show better conservation of the Hamiltonian in contrast to the Newtonian case which has a variation in the Hamiltonian of around 4×10^{-12}.

We confirm that the system is stable even after the inclusion of 2 and 2.5 PN corrections, see Fig. 6. In the Newtonian case the accumulation of numerical errors and probably a round-off in the initial parameters lead to a small variation of the orbits. The basic shape of the criss-cross figure suffers a small rotation. The 2 PN correction includes the effect of precession in the orbits; the original

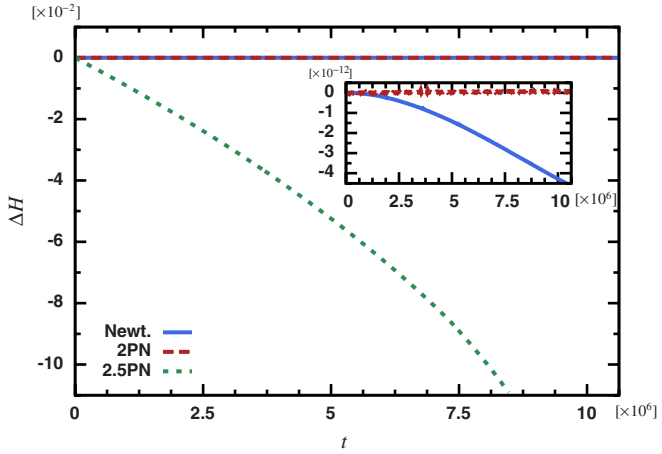

FIG. 5 (color online). Hénon criss-cross solution for Newtonian, 2 and 2.5 PN dynamics. The main panel shows the relative variation of the Hamiltonian for the three cases. The inset shows only the conservative systems (Newtonian and 2 PN).

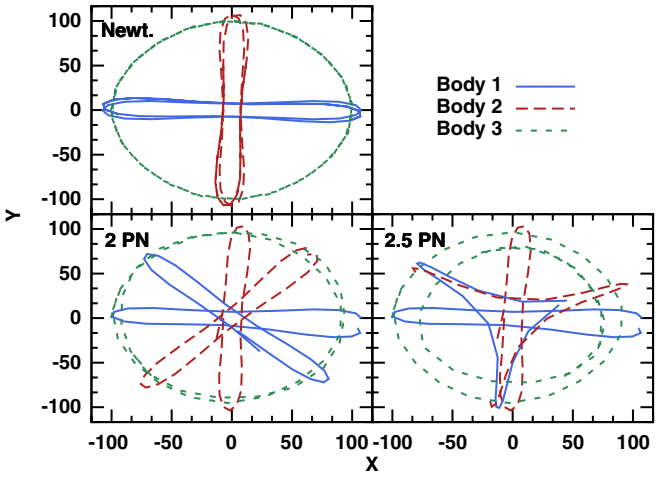

FIG. 6 (color online). Hénon criss-cross solution for Newtonian, 2 and 2.5 PN dynamics. First and last orbits. In the Newtonian dynamics the orbits do not show a significant change. For dynamics including 2 PN corrections the orbits exhibit the expected precession. For the dynamics which includes 2.5 PN corrections the gravitational radiation produces a significant change in the orbits which in the long run breaks the system.

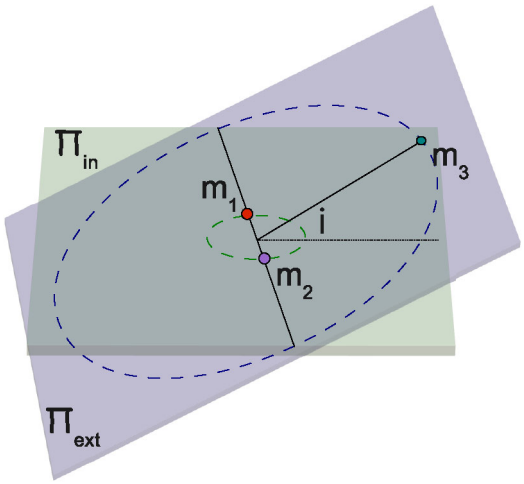

FIG. 7 (color online). Hierarchical system. Initial configuration of the inner and external binaries. The initial momentum of the third body is given by considering the external binary as a Newtonian binary. Shown are the osculating orbital planes $\Pi_{\rm in}$ and $\Pi_{\rm ext}$ for inner and external binary orbits. The two planes are inclined by an angle i.

figure spins many times around the origin preserving its original shape. The inclusion of gravitational radiation via the 2.5 PN corrections has a stronger effect on the orbits, slowly deforming the original figure. The body in the circularlike orbit shows a significant reduction of the orbital radius, the two other bodies follow at the end a triangular orbit with narrow corners.

We also use the Newtonian Hénon criss-cross solution for performance and accuracy tests. A performance test based on wall time measurements resulted in about 4.4 seconds per orbit on (one core of) an Intel i7-860 processor. For accuracy testing, we evaluate the error of time integration by a reversibility test. After computing a given number of orbits, we solve the system backward in time starting with the last position of each particle but replacing every linear momentum by its opposite value. To measure the error we compute the differences in phase space between the initial position and momentum and the position and momentum after the backward evolution. For our standard setting, the error after 100 orbits is on the order of 10^{-10}.

B. Strong perturbation of a binary system

Here we consider the strong perturbation of the dynamics and waveform of a binary compact object system due to a third smaller compact object. We take all PN corrections up to 2.5 PN for the three bodies. This approach gives us a good description of the third body orbiting close to the binary. However, the computational cost of each simulation increases with respect to the Newtonian simulations, making it too costly to perform a comprehensive study of this study. Nevertheless, we can select a representative case in an attempt to identify key properties.

As a basic configuration we study a Jacobian system with mass ratio 10:20:1. The inner binary system has initial separation $r_b(0) = 150$ and eccentricity $e_b(0) = 0$. We set the initial parameters considering only the Newtonian dynamics, in particular, the eccentricity refers to the Newtonian case. We view the third compact body and the center of mass of the inner binary as a new binary (we will refer to it as the external binary). The external binary has initial separation $r_3(0) = 10\,000$ and initial eccentricity $e_3(0) = 0$. The bodies start from a configuration where the apoapsis of the inner binary is perpendicular to the apoapsis of the external binary (see Fig. 7).

We denote the inclination angle between the osculating orbital planes $\Pi_{\rm in}$ and $\Pi_{\rm ext}$ by i (see Fig. 7). The behavior of the Hamiltonian is similar in every case that we consider. The conservative part of the Hamiltonian decreases relatively slowly during most of the simulation. However, when the system approaches the merger phase, the Hamiltonian decreases fast (see Fig. 8). As we mentioned before, the simulations are stopped when the contribution of the first post-Newtonian correction becomes larger than 10%. We consider this instant the time when the merger phase starts.

We consider five numerical experiments. In Table I we summarize the configurations of the numerical experiments. We vary one parameter of the basic configuration and fix the rest. The main goal of the study is to characterize the changes produced in the waveforms due to the change in each parameter.

1. Binary versus triple system

We compare the case where the inner binary is not being perturbed by the third compact body. Figure 9 shows the

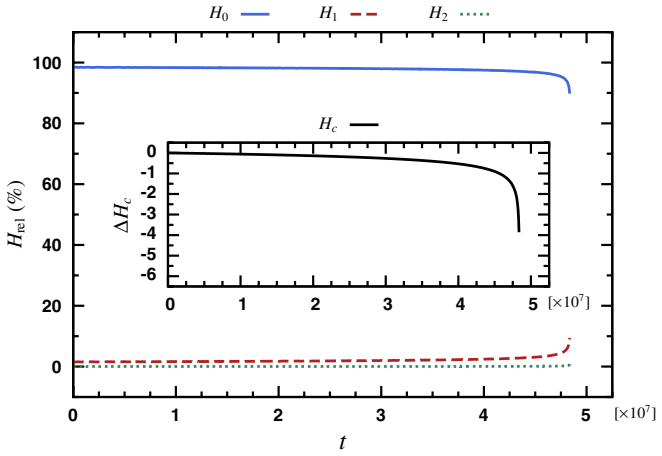

FIG. 8 (color online). Planar hierarchical system. Relative contribution to the Hamiltonian defined by (32). The inset shows the time dependence of $H_c = H_0 + H_1 + H_2$. Notice that when the system approaches the merger phase, the Hamiltonian decreases quickly.

components of the waveform for the h_+ polarization with an observational direction $\theta = \pi/4$, $\phi = 0$. In both cases the plot shows in light grey the mass quadrupole. The waveform looks like a shadow region because compared to the time scale of the entire evolution a single cycle looks like a very high frequency wave. In Fig. 9, the binary has completed 3448 orbits, while the inner binary of the triple system has completed 4071 orbits and the outer binary has completed 7.5 orbits. The mass octupole plus the current quadrupole MO + CQ are the dark region. Notice that in the triple system MO + CQ is modulated by the period of the third body (one cycle of modulation corresponds to half an orbit of the third body). The perturbation furthermore affects the merger time; for the triple system it takes more time for the inner binary to merge. We run the simulation for five initial inner binary separation $r_b \in \{130, 140, 150, 160, 170\}$. In Fig. 9 we mark with vertical

TABLE I. Configuration of the numerical experiments. The fixed parameters in each case are the mass ratio 10:20:1, the initial eccentricity of the inner binary $e_b = 0$, and the angle between the apoapsis of the inner binary and the apoapsis of the external binary which is set to $\pi/2$. The base configuration has initial binary separation $r_b = 150$, Hamiltonian $H_{0+1+2+2.5}$, eccentricity of the external binary $e_3 = 0$, inclination angle of the osculating planes $i = 0$ and initial external binary separation $r_3 = 10\,000$.

Experiment	Parameter variation
1	$r_b \in \{130, 140, 150, 160, 170\}$
2	$H \in \{H_{0+2.5}, H_{0+1+2.5}, H_{0+1+2+2.5}\}$
3	$e_3 \in \{0, 0.1, 0.2, 0.3, 0.4, 0.5, 0.6\}$
4	$i \in \{0, \pi/8, \pi/4, 3\pi/8, \pi/2\}$
5	$r_3 \in \{312.5, 625, 1250, 2500, 5000, 10\,000\}$

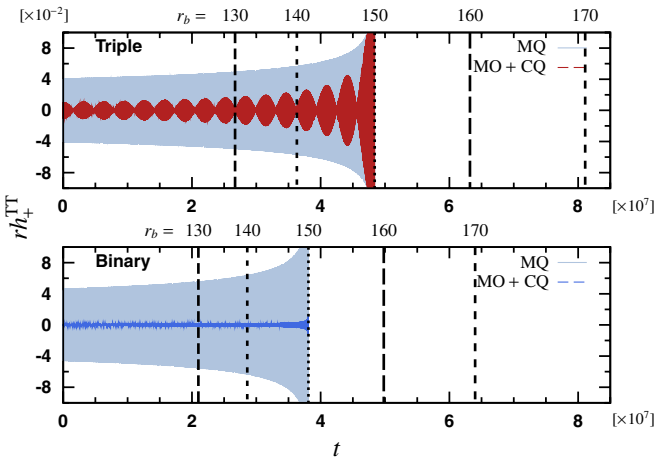

FIG. 9 (color online). Planar hierarchical system. Comparison between the perturbed binary and the unperturbed one. The light grey region is the mass quadrupole MQ contribution to the waveform rh_+, which is not resolved since there are 4070 orbits. The dark region inside the light grey one is the mass octupole plus the current quadrupole MO+CQ contribution to the waveform rh_+. The vertical lines mark the time when the simulations are stopped for initial separation $r_3 \in \{130, 140, 150, 160, 170\}$ of the inner binary.

lines the time at which the simulations are stopped. The relative change in the merger time

$$\frac{t_{3\rm BH} - t_{2\rm BH}}{t_{2\rm BH}} = 0.270 \pm 0.0025, \tag{37}$$

is almost constant for this simulation (the standard deviation is 0.0025). We did not observe any particular differences in the waveform when changing r_b.

2. Post-Newtonian corrections

In addition to the comparison to the nonperturbed binary system, we use the planar configuration to explore the influence of the conservative post-Newtonian corrections. As in the previous case with initial binary separation $r_b = 150$ (which we will denote as *full 2.5 PN* case), we solve the system for equations of motion where we remove the 2 PN part of the Hamiltonian (*radiative 1 PN*) and where we remove both 1 and 2 PN corrections (*radiative Newtonian*). The full 2.5 PN case does not show a big difference compared to the radiative 1 PN case. The merger phase time changes from $t = 4.8372 \times 10^7$ in the first case to $t = 4.8132 \times 10^7$ in the second one. The waveform does not suffer a noticeable change (see Fig. 10). On the other hand, in the radiative Newtonian case the result changes significantly. The merger phase time starts later than in previous cases (around $t = 5.6388 \times 10^7$). For this configuration dynamic which include the radiative 1 PN corrections seems to be a good approximation. However, for the rest of the simulations we employ the full 2.5 PN corrections.

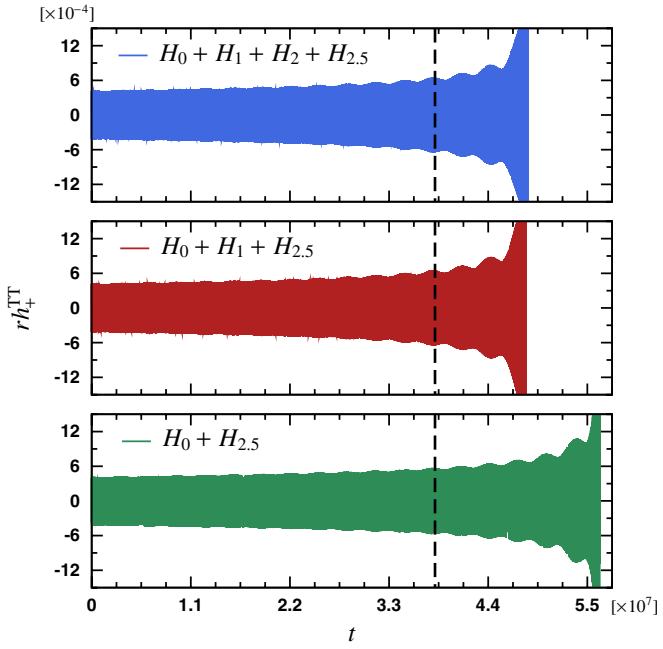

FIG. 10 (color online). Successive changes in the waveform due to post-Newtonian corrections. Waveform of a radiative Newtonian system (bottom), radiative 1 PN system (middle), and full 2.5 PN system (top). The waveform includes the current and mass quadrupole and the mass octupole contributions. The vertical dash line at $t = 3.81 \times 10^7$ marks the time when the nonperturbed binary system enters the merger phase (see Fig. 9).

3. Variation of the eccentricity of the external binary

We analyzed the variation of the waveform as a function of the eccentricity of the external binary e_3. We ran simulations for $e_3 \in \{0, 0.1, \ldots, 0.6\}$. In this case the response to the variation of the eccentricity is better reflected in the combination of $h^{l=2}_{m=1}$ and $h^{l=3}_{m=3}$. Figure 11 shows the sum of $l = 2, m = 1$ and $l = m = 3$ modes (which are the leading components of current quadrupole and mass octupole, respectively). The modulation of the modes shows two characteristic low-frequencies. If we divide the orbit of the external binary in two parts, one defined by the true anomaly[1] φ running from $\varphi = -\pi/2$ to $\varphi = \pi/2$ and the other by the complement $\varphi \in [\pi/2, 3\pi/2]$, it is possible to associate the characteristic frequencies to each part of the trajectory. We compute the envelope of the absolute value of the signal using a low-pass filter (dark line in Fig. 11) for 2/3 of the total signal (that part of the signal was easier to process for high eccentricity). Using the resulting function we compute numerically the local minima. The differences between minima are associated with the characteristic frequencies. An alternative way to extract the characteristic frequencies is by looking at the Fourier spectra of the filtered waveform.

[1]The true anomaly is defined as the angle which connects the periapsis, the main focus and the trajectory of the reduced body.

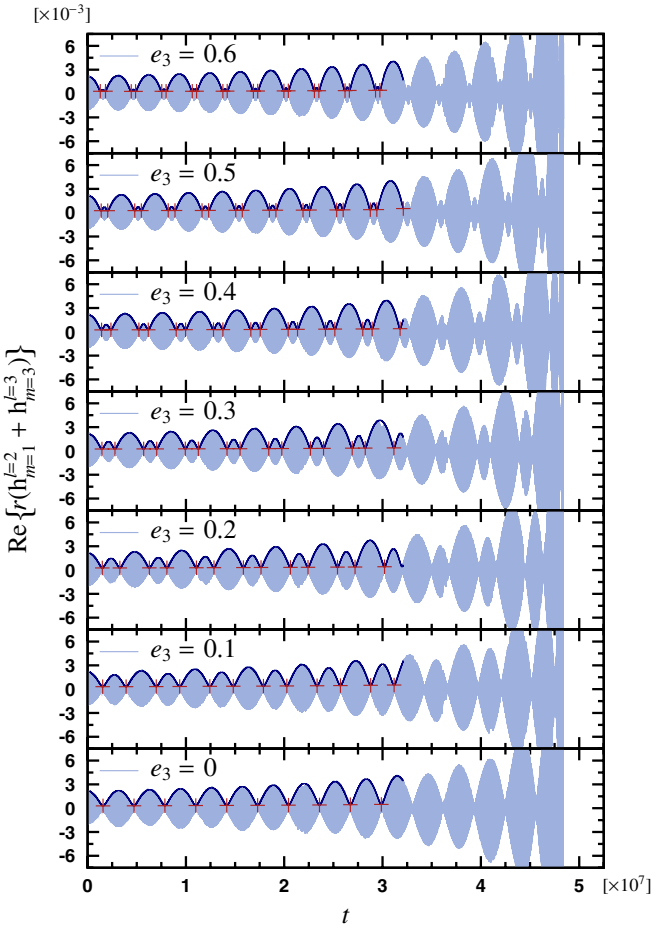

FIG. 11 (color online). Sum of modes $l = 2$, $m = 1$ and $l = m = 3$ as function of the eccentricity e_3. From bottom to top the variation of the modes for $e_e \in \{0, 0.1, \ldots, 0.6\}$. The dark line is the envelope of the function for 2/3 of the total simulation. The + marks are the local minima of the envelope.

We label the period for $\varphi \in [-\pi/2, \pi/2]$ as $\Delta t_{\rm ap}$ and the period for $\varphi \in [\pi/2, 3\pi/2]$ as $\Delta t_{\rm per}$ (at $\varphi = 0$ the external binary reaches the periapsis and at $\varphi = \pi$ the apoapsis). Table II shows the results, where we include the quotient.

In the Newtonian case it is possible to compute $\Delta t_{\rm ap}$ and $\Delta t_{\rm per}$ using the conservation of the angular

TABLE II. Periods $\Delta t_{\rm per}$ and $\Delta t_{\rm ap}$ and its quotient. The values are computed using the averages of the differences between the minima (see Fig. 11) and the errors by the standard deviation.

e_3	$\Delta t_{\rm per}[\times 10^6]$	$\Delta t_{\rm ap}[\times 10^6]$	$\Delta t_{\rm per}/\Delta t_{\rm ap}$
0	3.1473 ± 0.000 20	3.1427 ± 0.000 53	0.9985 ± 0.000 23
0.1	2.3812 ± 0.000 92	3.0700 ± 0.001 20	1.2890 ± 0.001 00
0.2	1.7890 ± 0.001 80	2.9950 ± 0.000 51	1.6750 ± 0.001 90
0.3	1.3260 ± 0.001 70	2.9160 ± 0.001 10	2.2000 ± 0.003 60
0.4	0.9590 ± 0.001 60	2.8370 ± 0.001 10	2.9580 ± 0.006 10
0.5	0.6690 ± 0.001 10	2.7530 ± 0.001 70	4.1180 ± 0.009 20
0.6	0.4390 ± 0.003 30	2.6670 ± 0.004 00	6.0700 ± 0.055 00

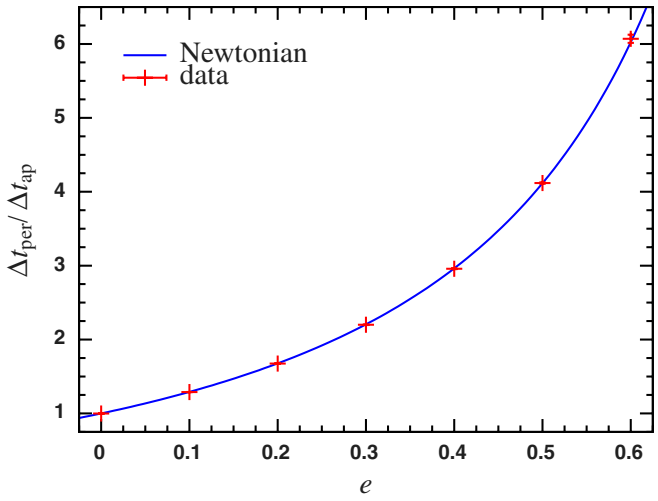

FIG. 12 (color online). Ratio of the periods $\Delta t_{\rm per}$ and $\Delta t_{\rm ap}$ as function of the eccentricity. The solid line shows the Newtonian relation.

momentum l and the equation of the orbit (see e.g. [57]). The result is

$$\Delta t_{\rm per} = \frac{l^3}{\mu}\int_{\pi/2}^{3\pi/2}(1+e\cos\varphi)^{-2}d\varphi, \tag{38}$$

$$\Delta t_{\rm ap} = \frac{l^3}{\mu}\int_{-\pi/2}^{\pi/2}(1+e\cos\varphi)^{-2}d\varphi, \tag{39}$$

where μ is the reduced mass of the binary. The quotient between the periods is related to the eccentricity by

$$\frac{\Delta t_{\rm per}}{\Delta t_{\rm ap}} = \frac{\pi}{2\arctan\sqrt{\frac{1-e}{1+e}} - e\sqrt{1-e^2}} - 1. \tag{40}$$

Figure 12 shows a comparison between the data presented in Table II and the Newtonian expression (40). For this case the Newtonian expression represents very well the functional behavior of our simulation.

4. Variation of the inclination angle

The period of modulation of the $l = 3$ modes of the waveform are related to the period of the third body. On the other hand, the amplitude of the $l = 3$ spherical components of the waveform encode information about the inclination angle i. We run simulations with the same initial configuration for $i \in \{0, \pi/8, \pi/4, 3\pi/8, \pi/2\}$. Figure 13 shows the variation of the amplitude for the real part of the modes $h^{l=3}_{m=2}$ and $h^{l=3}_{m=3}$ as function of i. Since the real and the imaginary part of the modes show the same behavior, for simplicity we present only the analysis of the real part. The real part of $h^{l=3}_{m=2}$ is zero for planar motion $i = 0$. However, the contribution of this mode increases with i. On the other hand, the contribution of $\mathrm{Re}\{h^{l=3}_{m=3}\}$ is maximal in the planar case and decreases when i increases. This behavior is symmetric with respect to $i = \pi/2$ and periodic with period π.

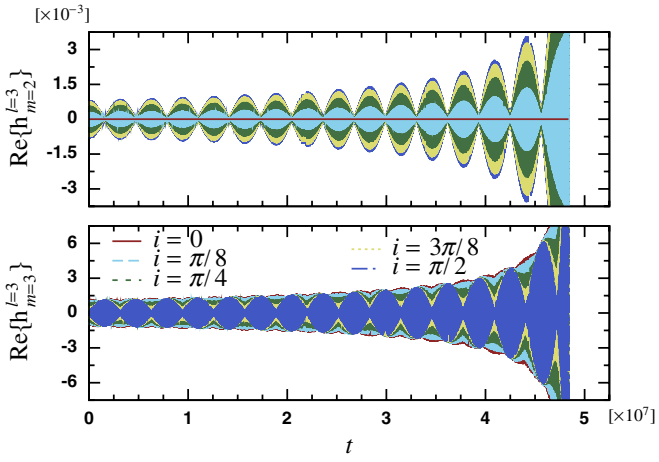

FIG. 13 (color online). Variation of the amplitude of $l = 3$, $m = 2$, 3, modes as a function of the inclination angle i. Superposition of $\mathrm{Re}\{h^{l=3}_{m=2}\}$ and $\mathrm{Re}\{h^{l=3}_{m=3}\}$ as function of i.

We estimate the contribution of each mode calculating the *area* which is covered by the real part of the mode,

$$\mathcal{A}^{l}_{m}(\tau) := -\int_{t_f}^{\tau} |\mathrm{Re}\{h^{l}_{m}(\bar{\tau})\}| d\bar{\tau}, \tag{41}$$

where $t_f = 4.8372 \times 10^7$ is the final time of the evolution and $\tau = t_f - t$. We integrate backward in time starting with the beginning of the merger phase at t_f. We compute $\mathcal{A}^{l}_{m}(t)$ for 8 uniformly spaced times during the simulation. We normalize the results using the maximum value $\mathcal{A}_{\rm max} = \mathcal{A}^{l=2}_{m=2}$. We denote the normalized area by A^{l}_{m}. As an example we show the results for $\tau = 0$ in Table III where we present the relevant modes. In total we compute 8 tables similar to the previous one, however for brevity we do not present them here. Notice that the contribution of the $l = 2$ modes is almost constant with respect to the inclination angle i. In Fig. 14 we show the variation of $A^{l=3}_{m=2}$ and $A^{l=3}_{m=3}$ for two integration times, $\tau = 0$ and $\tau = t_f/2$.

We found that the variation of $A^{l=3}_{m=2}$ is well represented by

$$A^{l=3}_{m=2}(t, i) = a(\tau)|\sin i|. \tag{42}$$

TABLE III. Variation of A^{l}_{m} as a function of the inclination angle i.

$\tau = 0$				A^{l}_{m}		
l	m	$i = 0$	$i = \pi/8$	$i = \pi/4$	$i = 2\pi/8$	$i = \pi/2$
2	0	0.0019	0.0019	0.0021	0.0024	0.0026
2	1	0.0000	0.0007	0.0013	0.0016	0.0018
2	2	1.0000	1.0000	1.0000	1.0000	1.0000
3	0	0.0000	0.0006	0.0021	0.0012	0.0544
3	1	0.0546	0.0527	0.0588	0.0397	0.1160
3	2	0.0000	0.0429	0.0799	0.1033	0.1583
3	3	0.2128	0.2052	0.1957	0.1552	0.2376

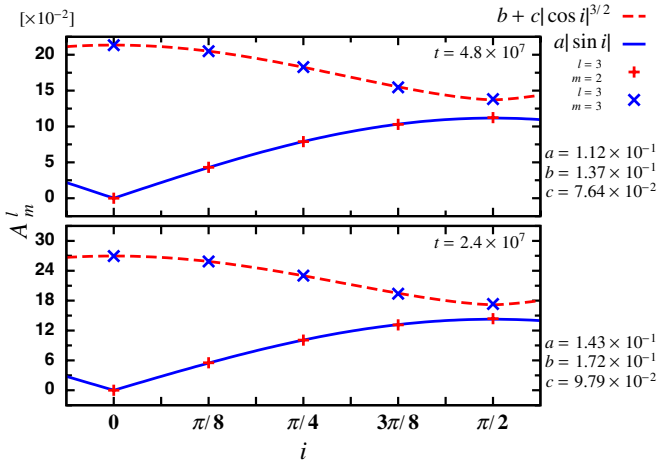

FIG. 14 (color online). Variation of A^l_m as a function of i for $t = t_f$ (upper panel) and $t = t_f/2$ (lower panel).

On the other hand, $A^{l=3}_{m=3}$ is well modeled by

$$A^{l=3}_{m=3}(t, i) = b(\tau) + c(\tau)|\cos i|^{3/2}, \tag{43}$$

where the fitting coefficients a, b and c depend on the interval of integration. Table IV shows the fitting coefficients as a function of the integration time τ. From this data it is possible to fit a function to establish the functional behavior of the coefficients with respect to the integration time. The result is shown in Fig. 15. The coefficients a, b and c are well represented by

$$a(\tau) = \alpha_1 e^{-\tau^{\alpha_2}}, \tag{44}$$

$$b(\tau) = \beta_1 e^{-\tau^{\beta_2}}, \tag{45}$$

$$c(\tau) = \gamma_1 e^{-\tau^{\gamma_2}}, \tag{46}$$

where

$$\alpha_1 = 8.94 \pm 0.018, \tag{47}$$

$$\alpha_2 = (8.352 \pm 0.0029) \times 10^{-2}, \tag{48}$$

$$\beta_1 = 10.17 \pm 0.21, \tag{49}$$

TABLE IV. Fitting coefficients of Eqns. (42) and (43). For the 8 time intervals we compute the fitting coefficients a, b and c. We include the error of each coefficient.

$\tau[\times 10^7]$	$a(\tau)[\times 10^{-2}]$	$b(\tau)[\times 10^{-2}]$	$c(\tau)[\times 10^{-2}]$
0.6047	22.45 ± 0.066	26.99 ± 0.116	15.21 ± 0.171
1.2093	18.04 ± 0.035	21.57 ± 0.062	12.28 ± 0.092
1.8140	15.76 ± 0.025	18.90 ± 0.046	10.75 ± 0.067
2.4186	14.28 ± 0.019	17.19 ± 0.036	9.76 ± 0.054
3.0233	13.21 ± 0.016	15.99 ± 0.031	9.03 ± 0.046
3.6279	12.38 ± 0.014	15.07 ± 0.027	8.47 ± 0.041
4.2326	11.72 ± 0.012	14.33 ± 0.025	8.00 ± 0.037
4.8372	11.18 ± 0.011	13.73 ± 0.024	7.62 ± 0.035

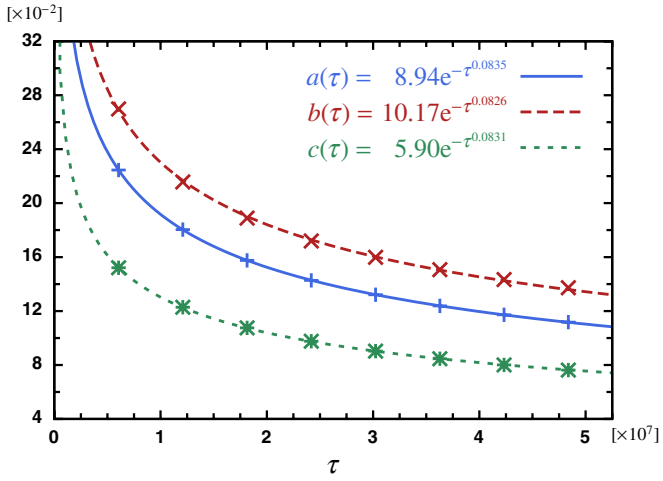

FIG. 15 (color online). Functional behavior of the fitting coefficients. The coefficients are well described by an exponential decay function in τ.

$$\beta_2 = (8.26 \pm 0.032) \times 10^{-2}, \tag{50}$$

$$\gamma_1 = 5.90 \pm 0.033, \tag{51}$$

$$\gamma_2 = (8.305 \pm 0.0084) \times 10^{-2}. \tag{52}$$

The asymptotic behavior of the coefficients suggests that for long integration times it is possible to consider them as constants.

Alternatively, it is possible to relate the inclination angle i with the maximum of the modes $l = 3$, $m = 2$ and $l = 2$, $m = 1$. As in Sec. III B 3, we compute the envelope of the modes using a low-pass filter. The upper panel in Fig. 16 shows the result for the angle $i = \pi/4$. The quotient of the

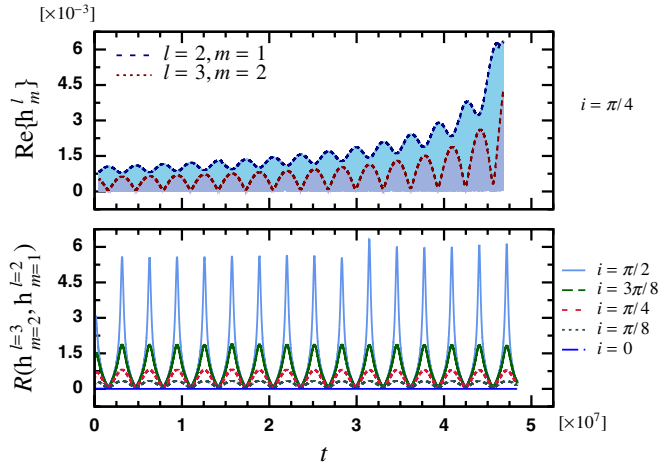

FIG. 16 (color online). Variation of modes $l = 3$, $m = 2$ and $l = 2$, $m = 1$ as a function of the inclination angle i. The upper panel shows for $i = \pi/4$ the absolute value of the modes and its envelope. The lower panel shows the quotient of the envelopes $l = 3$, $m = 2$ and $l = 2$, $m = 1$. Notice that the resulting function is almost periodic and does not show the characteristic growth close to the merger phase.

TABLE V. The maximum of (53) as a function of the inclination angle i. Listed is the average value of the maxima, while the error is given by the standard deviation of the data.

i	Max$[R(\mathrm{h}^{l=3}_{m=2}, \mathrm{h}^{l=2}_{m=1})]$	Variation (%)
0	0	0
$\pi/16$	$0.1608 \pm 0.000\,77$	0.48
$\pi/8$	0.335 ± 0.0012	0.36
$3\pi/16$	0.538 ± 0.0029	0.54
$\pi/4$	0.806 ± 0.0049	0.61
$5\pi/16$	1.193 ± 0.0056	0.47
$3\pi/8$	1.864 ± 0.0093	0.50
$7\pi/16$	3.41 ± 0.026	0.75
$\pi/2$	5.57 ± 0.033	0.60

envelope of the modes $l = 3$, $m = 2$ and $l = 2$, $m = 1$ gives a periodic function which removes the growth of the modes close to the merger time. We define the function R which *rectifies* the envelopes as

$$R(\mathrm{h}^{l=3}_{m=2}, \mathrm{h}^{l=2}_{m=1}) := \frac{\mathrm{Env}[\mathrm{Re}\{\mathrm{h}^{l=3}_{m=2}\}]}{\mathrm{Env}[\mathrm{Re}\{\mathrm{h}^{l=2}_{m=1}\}]}. \tag{53}$$

The lower panel of Fig. 16 shows the result of applying (53) to our data. Notice that in the case of $i = \pi/2$ the values after $t = 3 \times 10^7$ are a little erratic. For our analysis we consider for $i = \pi/2$ only the points before $t = 3 \times 10^7$.

From the resulting function we compute numerically the local maxima of (53). Table V shows the result. For this purpose we perform additional simulations for angles $\pi/16$, $3\pi/16$, $5\pi/16$ and $7\pi/16$. We fit to the data the function $f(i) = a i e^{b i^2}$, where $a = 0.65 \pm 0.034$ and $b = 0.69 \pm 0.024$. Figure 17 shows the result, notice that the functional behavior is well represented by the fitted function.

In both cases, using the relative "area" of the modes or the maximum of the "rectified" modes, we obtain quite a simple behavior. The advantage of the second method is that it does not depend on the integration time τ.

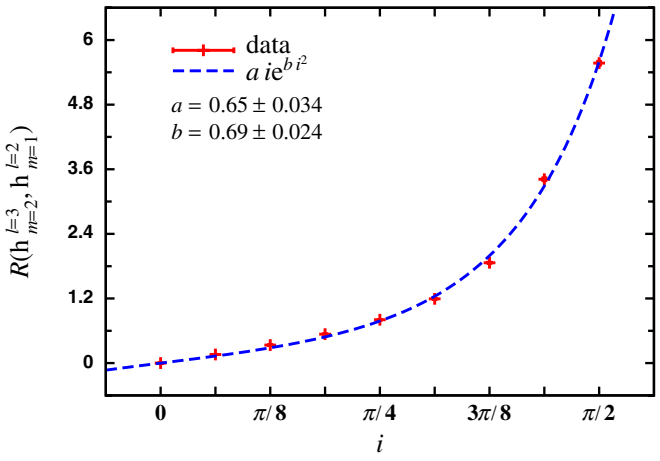

FIG. 17 (color online). The maximum of (53) as a function of the inclination angle i. The functional behavior is well represented by the function $a i e^{b i^2}$.

5. Initial separation of the external binary

The last numerical experiment examines the dependence on the initial separation of the external binary r_3. We set the value of r_3 to 312.5, 625, 1250, 2500, 5000, and 10 000. For $r_3 = 312.5$ the external body is ejected from the binary after a few orbits, the other configurations are stable.

Figure 18 shows the sum of the mass octupole and current quadrupole contributions to the waveform. The frequency of the modulation of the waveform increases when the separation and hence the orbital period of the external binary is decreased. One orbit of the external binary corresponds to the time between two of the nodes of the mass octupole plus current quadrupole contribution shown in Fig. 18. The influence of a third body is not clearly defined when the period of the external binary is similar to the inner binary. For small separations, on the scale shown there is no modulation of the waves visible (see Fig. 18 (a) and (b)). When the initial separation of the external binary is increased, at some distance most of the inspiral and merger of the inner binary happens before the external binary completes one orbit.

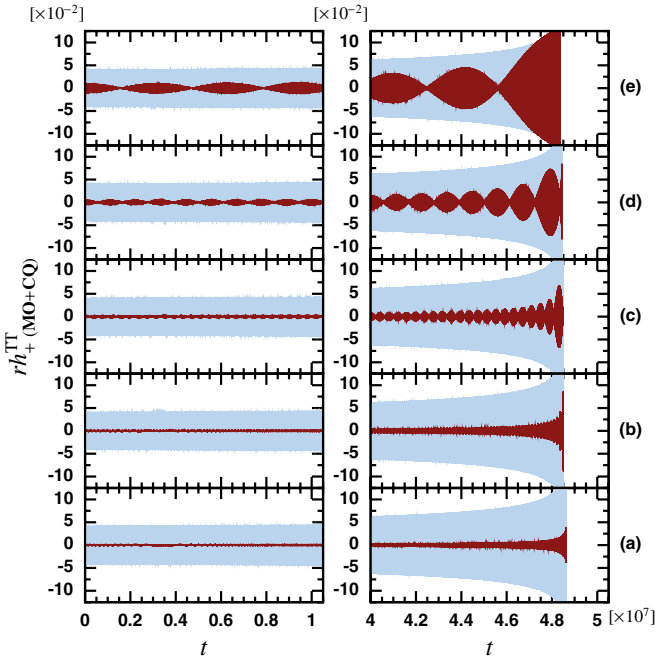

FIG. 18 (color online). Planar hierarchical system. Modulation of the mass octupole plus the current quadrupole as function of the initial separation of the external body. The initial separation r_3 takes the values 625 (a), 1250 (b), 2500 (c), 5000 (d) and 10 000 (e). Shown on the left is the evolution for $t \in [0, 10^7]$ and on the right for $t \in [4 \times 10^7, 5 \times 10^7]$.

VI. DISCUSSION

We performed post-Newtonian simulations for a selection of hierarchical configurations as an example for a three-body system, and we analyzed the waveforms. Based on these simulations we examined a number of different physical aspects of the system.

First of all, looking at the mass octupole and current quadrupole part of the waveform, it is possible to distinguish between such a hierarchical (also called Jacobian) triple system and a binary system, an issue that has been discussed in [2,3].

In terms of the merger time, the perturbed binary merges later. For mass ratio 10:20:1, the delay of the merger is 27% compared to the binary with 10:20, which is perhaps surprisingly large. However, let us note that even a small perturbation due to a third object can have a large effect when integrated over about 4000 orbits of the inner binary (i.e. there is less than a 0.01% delay per orbit). As we have shown, the delay depends only very weakly on the inclination angle or the distance to the third body, see Figs. 13 and 18. This may be expected since the force due to the third body periodically increases but also decreases the force between the objects of the inner binary (depending on the orientation of the binary with respect to the third body), which apparently averages out over several orbits of the inner binary. As a cross check we also performed simulations where the third mass approaches zero, and in this case the merger time does approach that of the binary.

As far as the approximation method is concerned, we find that there is a significant difference in the merger time for a system which includes Newtonian dynamics and 2.5 PN radiation compared to the inclusion of 1 PN or 2 PN corrections to the dynamics. The inclusion of 1 PN corrections to the conservative part of the Hamiltonian produces a change of 16% in the merger time. However, the inclusion of 2 PN corrections does not make a significant difference to either the waveform or the merger time (only around 0.5%).

The variation of the eccentricity of the external binary shows that the period of the third body is well described by the Newtonian dynamics. From the modulation of the waveform modes (particularly from the sum of the $l = 2$, $m = 1$ and $l = m = 3$ modes), it is possible to distinguish two frequencies which are related to the eccentricity via a Newtonian expression.

We established a link between the amplitude of the $l = 3$, $m = 2$ and $l = m = 3$ modes and the angle of the osculating orbital planes. In order to extract the information given by the waves we used two methods. First, we used the relative area covered by the $l = 3$, $m = 2$ and $l = m = 3$ modes with respect to the area covered by the mode $l = m = 2$. In this case the contribution of the $l = 3$, $m = 2$ mode is particularly simple. It is zero for planar motion and increases as a sine function of the inclination angle. The second method is based on the quotient of the envelope of the $l = 3$, $m = 2$ mode and the envelope of the $l = 2$, $m = 1$ mode. The resulting function is almost periodic and does not contain the characteristic growth of the waveforms close to the merger phase. In this case, it is possible to relate the inclination angle to the amplitude of the resulting function. The modulation produced by the third body on the $l = 3$ modes characterizes the period of the external binary. Decreasing the initial separation of the external body produces a higher frequency modulation, until it is no longer possible to discern a well defined modulation of the waveform. In our simulations, when there are no well defined internal and external binaries the system is not stable.

Our results provide additional evidence to a conjecture first stated in [2], that in order to characterize a system of n compact objects, it is necessary to perform an analysis of the waveform which includes at least the $l \leq n$ modes. As we showed in the last numerical experiment, when the third body is close to the binary it is not evident how to extract information related to the dynamics of a particular body. It is necessary to perform a detailed study of non-hierarchical triple systems to determine how much information we can extract from more general cases. More detailed statements based on the higher modes of the waveform are possible but require an extensive parameter study. Other configurations include, for example, a massive compact object perturbing a binary, or the scattering and capture of a third body. The present examples showed the type of characterization that are possible with the techniques developed above.

As a final comment, let us point out that chaotic behavior of triple systems is well known in the Newtonian case (see e.g. [4] and references therein). For binaries, it is known that chaos appears when using certain post-Newtonian approximations for systems of *spinning* binaries (see e.g. [62–68]). As a natural generalization of the Newtonian case we expect that the three-body problem exhibits chaotic behavior as well. An important question is, how does the emission of gravitational radiation change the chaotic properties of the system? We consider this a topic for future study.

ACKNOWLEDGMENTS

It is a pleasure to thank Gerhard Schäfer, Sebastiano Bernuzzi, David Hilditch, and Milton Ruiz for valuable discussions and comments on the manuscript. This work was supported in part by DFG Grant SFB/Transregio 7 and by a DLR grant, LISA Germany.

APPENDIX A: FIRST AND SECOND POST-NEWTONIAN HAMILTONIAN

Here we reproduce in our notation the Hamiltonian given in [34], with some factorizations and changes in the summation of the terms T1 and T2, which are marked

by braces below. Our version (worked out with G. Schäfer) fixes the typos noted in [35], giving a formula equivalent to [35] but written in a different way. The issue is how the four-point functions of [37] are reduced to explicit triple sums for a three-body problem. The first and second post-Newtonian Hamiltonians are

$$H_1 = -\frac{1}{8}\sum_a m_a\left(\frac{\vec{p}_a^2}{m_a^2}\right)^2 - \frac{1}{4}\sum_a\sum_{b\neq a}\frac{1}{r_{ab}}\left(6\frac{m_b}{m_a}\vec{p}_a^2 - 7\vec{p}_a\cdot\vec{p}_b - (\hat{n}_{ab}\cdot\vec{p}_a)(\hat{n}_{ab}\cdot\vec{p}_b)\right) + \frac{1}{2}\sum_a\sum_{b\neq a}\sum_{c\neq a}\frac{m_a m_b m_c}{r_{ab}r_{ac}}, \tag{A1}$$

$$\begin{aligned}
H_2 = {} & \frac{1}{16}\sum_a m_a\left(\frac{\vec{p}_a^2}{m_a^2}\right)^3 + \frac{1}{16}\sum_a\sum_{b\neq a}\frac{m_a^{-1}m_b^{-1}}{r_{ab}}\Big[10\left(\frac{m_b}{m_a}\vec{p}_a^2\right)^2 - 11\vec{p}_a^2\vec{p}_b^2 - 2(\vec{p}_a\cdot\vec{p}_b)^2 + 10\vec{p}_a^2(\hat{n}_{ab}\cdot\vec{p}_b)^2 \\
& - 12(\vec{p}_a\cdot\vec{p}_b)(\hat{n}_{ab}\cdot\vec{p}_a)(\hat{n}_{ab}\cdot\vec{p}_b) - 3(\hat{n}_{ab}\cdot\vec{p}_a)^2(\hat{n}_{ab}\cdot\vec{p}_b)^2\Big] + \frac{1}{8}\sum_a\sum_{b\neq a}\sum_{c\neq a}\frac{1}{r_{ab}r_{ac}}\Big[18\frac{m_b m_c}{m_a}\vec{p}_a^2 + 14\frac{m_a m_c}{m_b}\vec{p}_b^2 \\
& - 2\frac{m_a m_c}{m_b}(\hat{n}_{ab}\cdot\vec{p}_b)^2 - 50m_c(\vec{p}_a\cdot\vec{p}_b) + 17m_a(\vec{p}_b\cdot\vec{p}_c) - 14m_c(\hat{n}_{ab}\cdot\vec{p}_a)(\hat{n}_{ab}\cdot\vec{p}_b) + 14m_a(\hat{n}_{ab}\cdot\vec{p}_b)(\hat{n}_{ab}\cdot\vec{p}_c) \\
& + m_a(\hat{n}_{ab}\cdot\hat{n}_{ac})(\hat{n}_{ab}\cdot\vec{p}_b)(\hat{n}_{ac}\cdot\vec{p}_c)\Big] + \frac{1}{8}\sum_a\sum_{b\neq a}\sum_{c\neq a}\frac{1}{r_{ab}^2}\Big[2m_b(\hat{n}_{ab}\cdot\vec{p}_a)(\hat{n}_{ac}\cdot\vec{p}_c) + 2m_b(\hat{n}_{ab}\cdot\vec{p}_b)(\hat{n}_{ac}\cdot\vec{p}_c) \\
& + \frac{m_a m_b}{m_c}(5(\hat{n}_{ab}\cdot\hat{n}_{ac})\vec{p}_c^2 - (\hat{n}_{ab}\cdot\hat{n}_{ac})(\hat{n}_{ac}\cdot\vec{p}_c)^2 - 14(\hat{n}_{ab}\cdot\vec{p}_c)(\hat{n}_{ac}\cdot\vec{p}_c))\Big] + \frac{1}{4}\sum_a\sum_{b\neq a}\frac{m_a}{r_{ab}^2}\Big[\frac{m_b}{m_a}\vec{p}_a^2 + \frac{m_a}{m_b}\vec{p}_b^2 \\
& - 2(\vec{p}_a\cdot\vec{p}_b)\Big] + \frac{1}{2}\sum_a\sum_{b\neq a}\sum_{c\neq a,b}\frac{(n_{ab}^i + n_{ac}^i)(n_{ab}^j + n_{cb}^j)}{(r_{ab}+r_{bc}+r_{ca})^2}[8m_b(p_{ai}p_{cj}) - 16m_b(p_{aj}p_{ci}) + 3m_c(p_{ai}p_{bj}) \\
& + 4\frac{m_a m_b}{m_c}(p_{ci}p_{cj}) + \frac{m_b m_c}{m_a}(p_{ai}p_{aj})\Big] + \frac{1}{2}\sum_a\sum_{b\neq a}\sum_{c\neq a,b}\frac{m_a m_b m_c}{(r_{ab}+r_{bc}+r_{ca})r_{ab}}\Big[8\frac{\vec{p}_a\cdot\vec{p}_c - (\hat{n}_{ab}\cdot\vec{p}_a)(\hat{n}_{ab}\cdot\vec{p}_c)}{m_a m_c} \\
& - 3\frac{\vec{p}_a\cdot\vec{p}_b - (\hat{n}_{ab}\cdot\vec{p}_a)(\hat{n}_{ab}\cdot\vec{p}_b)}{m_a m_b} - 4\frac{\vec{p}_c^2 - (\hat{n}_{ab}\cdot\vec{p}_c)^2}{m_c^2} - \frac{\vec{p}_a^2 - (\hat{n}_{ab}\cdot\vec{p}_a)^2}{m_a^2}\Big] \\
& \overbrace{- \frac{1}{2}\sum_a\sum_{b\neq a}\Big(\sum_{c\neq a,b}\frac{m_a^2 m_b m_c}{r_{ab}^2 r_{bc}} + \frac{1}{2}\sum_{c\neq b}\frac{m_a^2 m_b m_c}{r_{ab}^2 r_{bc}}\Big)}^{\mathrm{T1}} \overbrace{- \frac{3}{8}\sum_a\sum_{b\neq a}\Big(\sum_{c\neq a}\frac{m_a^2 m_b m_c}{r_{ab}^2 r_{ac}} + \sum_{c\neq a,b}\frac{m_a^2 m_b m_c}{r_{ab}^2 r_{ac}}\Big)}^{\mathrm{T2}} \\
& - \frac{3}{8}\sum_a\sum_{b\neq a}\sum_{c\neq a,b}\frac{m_a^2 m_b m_c}{r_{ab}^2 r_{ac} r_{bc}} - \frac{1}{64}\sum_a\sum_{b\neq a}\sum_{c\neq a,b}\frac{m_a^2 m_b m_c}{r_{ab} r_{ac}^3 r_{bc}}\Big\{18r_{ac}^2 - 60r_{bc}^2 - 24r_{ac}(r_{ab}+r_{bc}) \\
& + 60\frac{r_{ac}r_{bc}^2}{r_{ab}} + 56r_{ab}r_{bc} - 72\frac{r_{bc}^3}{r_{ab}} + 35\frac{r_{bc}^4}{r_{ab}^2} + 6r_{ab}^2\Big\} - \frac{1}{4}\sum_a\sum_{b\neq a}\frac{m_a^2 m_b^2}{r_{ab}^3}.
\end{aligned} \tag{A2}$$

APENDIX B: LAGRANGE TRIANGLE SOLUTION WAVEFORM

Here we sumarize the expressions for the mass quadrupole, mass octupole, and current quadrupole waveforms for each polarization of the Lagrange triangle solution. See [3] for details on the calculation of this expression. We denote by $a := r_{12} = r_{13} = r_{23}$ the separation between each pair of bodies. m_1, m_2 and m_3 are the dimensionless mass parameters, $\omega = a^{-3/2}$ is the orbital frequency, r is the distance from the observer to the source and θ is the observational direction. We define the following auxiliary quantities:

$$\mu_i := \sqrt{m_j^2 + m_j m_k + m_k^2}, \tag{B1}$$

$$\phi_1 := 0, \tag{B2}$$

$$\phi_2 := \arccos\left(\frac{\mu_1^2 + \mu_3^2 - 1}{2\mu_1\mu_3}\right), \tag{B3}$$

$$\phi_3 := -\arccos\left(\frac{\mu_1^2 + \mu_2^2 - 1}{2\mu_1\mu_2}\right), \tag{B4}$$

where $j \neq i, k \neq i, j$. The plus and cross polarizations of the mass quadrupole waveform are

$$rh_+^{\mathrm{MQ}} = -(3 + \cos 2\theta)a^2\omega^2\sum_{i=1}^{3} m_i\mu_i^2\cos(2(\omega t + \phi_i)), \tag{B5}$$

$$rh_{\times}^{\mathrm{MQ}} = -4\cos\theta a^2\omega^2 \sum_{i=1}^{3} m_i\mu_i^2 \sin(2(\omega t + \phi_i)), \quad \text{(B6)}$$

the expressions for the current quadrupole are

$$rh_{+}^{\mathrm{CQ}} = \frac{4a^3\omega^3}{3} \sin\theta \sum_{i=1}^{3} m_i\mu_i^3 \cos(\omega t + \phi_i), \quad \text{(B7)}$$

$$rh_{\times}^{\mathrm{CQ}} = \frac{2a^3\omega^3}{3} \sin(2\theta) \sum_{i=1}^{3} m_i\mu_i^3 \sin(\omega t + \phi_i), \quad \text{(B8)}$$

and the waveforms for the mass octupole are given by

$$rh_{+}^{\mathrm{MO}} = \frac{a^3\omega^3}{12} \sin\theta \sum_{i=1}^{3} m_i\mu_i^3[(3\cos^2\theta - 1)\cos(\omega t + \phi_i) - (27(1 + \cos^2\theta))\cos(3(\omega t + \phi_i))] \quad \text{(B9)}$$

$$rh_{\times}^{\mathrm{MO}} = \frac{a^3\omega^3}{12} \sin(2\theta) \sum_{i=1}^{3} m_i\mu_i^3[\sin(\omega t + \phi_i) - 27\sin(3(\omega t + \phi_i))] \quad \text{(B10)}$$

[1] T. Chiba, T. Imai, and H. Asada, Mon. Not. R. Astron. Soc. **377**, 269 (2007).
[2] Y. Torigoe, K. Hattori, and H. Asada, Phys. Rev. Lett. **102**, 251101 (2009).
[3] H. Asada, Phys. Rev. D **80**, 064021 (2009).
[4] M. J. Valtonen and H. Karttunen, *The three-body Problem* (Cambridge University Press, New York, 2006), ISBN 0-521-85224-2 (hardcover).
[5] K. Gultekin, M. C. Miller, and D. P. Hamilton, in *The Astrophysics of Gravitational Wave Sources*, edited by Joan M. Centrella and Sandy Barnes, AIP Conf. Proc. No. 686 (AIP, New York, 2003).
[6] K. Gultekin, M. C. Miller, and D. P. Hamilton, Astrophys. J. **616**, 221 (2004).
[7] K. Gultekin, M. C. Miller, and D. P. Hamilton, Astrophys. J. **640**, 156 (2006).
[8] M. Iwasawa, Y. Funato, and J. Makino, Astrophys. J. **651**, 1059 (2006).
[9] L. Homan and A. Loeb, Mon. Not. R. Astron. Soc. **377**, 957 (2007).
[10] L. Homan and A. Loeb, Astrophys. J. **638**, L75 (2006).
[11] A. Gualandris, S. Portegies Zwart, and M. S. Sipior, Mon. Not. R. Astron. Soc. **363**, 223 (2005).
[12] S. Mikkola, Mon. Not. R. Astron. Soc. **203**, 1107 (1983), http://adsabs.harvard.edu/abs/1983MNRAS.203.1107M.
[13] S. Mikkola, Mon. Not. R. Astron. Soc. **207**, 115 (1984), http://adsabs.harvard.edu/abs/1984MNRAS.207..115M.
[14] M. C. Miller and D. P. Hamilton, Astrophys. J. **576**, 894 (2002).
[15] P. Heinamaki, Astron. Astrophys. **371**, 795 (2001).
[16] M. Valtonen and S. Mikkola, Annu. Rev. Astron. Astrophys. **29**, 9 (1991).
[17] M. Campanelli, C. O. Lousto, and Y. Zlochower, Phys. Rev. D **77**, 101501(R) (2008).
[18] C. O. Lousto and Y. Zlochower, Phys. Rev. D **77**, 024034 (2008).
[19] P. Galaviz, B. Brugmann, and Z. Cao, Phys. Rev. D **82**, 024005 (2010).
[20] P. Diener, Classical Quantum Gravity **20**, 4901 (2003).
[21] G. Jaramillo and C. O. Lousto, arXiv:1008.2001.
[22] M. Ponce, C. Lousto, and Y. Zlochower, arXiv:1008.2761.
[23] T. Damour, P. Jaranowski, and G. Schafer, Phys. Rev. D **77**, 064032 (2008).
[24] J. Steinho, S. Hergt, and G. Schafer, Phys. Rev. D **77**, 081501 (2008).
[25] J. Hartung and J. Steinho, Phys. Rev. D **83**, 044008 (2011).
[26] P. Jaranowski and G. Schafer, Phys. Rev. D **55**, 4712 (1997).
[27] L. Blanchet, Living Rev. Relativity **9**, 1 (2006), http://www.livingreviews.org/lrr-2006-4.
[28] T. Futamase and Y. Itoh, Living Rev. Relativity **10**, 1 (2007), http://www.livingreviews.org/lrr-2007-2.
[29] T. Damour, P. Jaranowski, and G. Schafer, Phys. Rev. D **62**, 021501 (2000).
[30] T. Damour, P. Jaranowski, and G. Schafer, Phys. Rev. D **63**, 044021 (2001).
[31] T. Damour, P. Jaranowski, and G. Schafer, Phys. Lett. B **513**, 147 (2001).
[32] L. Blanchet, T. Damour, and G. Esposito-Farese, Phys. Rev. D **69**, 124007 (2004).
[33] C. Konigsdorer, G. Faye, and G. Schafer, Phys. Rev. D **68**, 044004 (2003).
[34] G. Schafer, Phys. Lett. A **123**, 336 (1987).
[35] C. O. Lousto and H. Nakano, Classical Quantum Gravity **25**, 195019 (2008).
[36] Y. Chu, Phys. Rev. D **79**, 044031 (2009).
[37] T. Ohta, T. Kimura, and K. Hiida, Nuovo Cimento Soc. Ital. Fis. B **27**, 103 (1975).
[38] T. Mitchell and C. M. Will, Phys. Rev. D **75**, 124025 (2007).
[39] C. Moore, Phys. Rev. Lett. **70**, 3675 (1993).
[40] T. Imai, T. Chiba, and H. Asada, Phys. Rev. Lett. **98**, 201102 (2007).
[41] K. Yamada and H. Asada, Phys. Rev. D **82**, 104019 (2010).
[42] K. Yamada and H. Asada, Phys. Rev. D **83**, 024040 (2011).
[43] T. Ichita, K. Yamada, and H. Asada, arXiv:1011.3886.
[44] J. D. Schnittman, Astrophys. J. **724**, 39 (2010).
[45] P. Amaro-Seoane and M. Dewi Freitag, arXiv:1009.1870 [Mon. Not. R. Astron. Soc. (to be published)].
[46] J. Levin and H. Contreras, arXiv:1009.2533.

[47] T. Szirtes, *Applied Dimensional Analysis and Modeling* (Butterworth-Heinemann, Oxford, UK, 2006), 2nd ed..
[48] M. Maggiore, *Gravitational Waves* (Oxford University Press, New York, 2007), Vol. 1.
[49] T. Damour and G. Schafer, Gen. Relativ. Gravit. **17**, 879 (1985).
[50] E. E. Flanagan and S. A. Hughes, New J. Phys. **7**, 204 (2005).
[51] Wolfram Research, Inc., MATHEMATICA, version 7.0 ed. (Wolfram Research, Inc., Champaign, IL, 2008).
[52] C. A. Burdet, Zeitschrift Angewandte Mathematik und Physik **18**, 434 (1967).
[53] D. C. Heggie, Celest. Mech. **10**, 217 (1974).
[54] S. Mikkola and S. J. Aarseth, Celest. Mech. Dyn. Astron. **47**, 375 (1990).
[55] S. Mikkola and S. J. Aarseth, Celest. Mech. Dyn. Astron. **57**, 439 (1993).
[56] S. Mikkola and S. J. Aarseth, Celest. Mech. Dyn. Astron. **64**, 197 (1996).
[57] H. Goldstein, C. P. Poole, and J. Safko, *Classical Mechanics* (Addison Wesley, New York, 2001), .
[58] P. C. Peters, Phys. Rev. **136**, B1224 (1964).
[59] M. Henon, Celest. Mech. **13**, 267 (1976).
[60] M. Nauenberg, Phys. Lett. A **292**, 93 (2001).
[61] C. Moore and M. Nauenberg, arXiv:math/0511219v2.
[62] J. Levin, Phys. Rev. Lett. **84**, 3515 (2000).
[63] N. J. Cornish and J. Levin, Phys. Rev. D **68**, 024004 (2003).
[64] J. D. Barrow and J. Levin, arXiv:nlin/0303070.
[65] J. Levin, Phys. Rev. D **74**, 124027 (2006).
[66] A. Gopakumar and C. Konigsdorer, Phys. Rev. D **72**, 121501 (2005).
[67] W. Han, Gen. Relativ. Gravit. **40**, 1831 (2008).
[68] J. D. Schnittman and F. A. Rasio, Phys. Rev. Lett. **87**, 121101 (2001).